Elucidating polymorphs of crystal structures with intensity-based hierarchical clustering analysis on multiple diffraction datasets

Hiroaki Matsuura,[a] Naoki Sakai,[a,b] Sachiko Toma-Fukai,[c,d] Norifumi Muraki,[e,f‡] Koki Hayama,[c] Hironari Kamikubo,[c] Shigetoshi Aono,[e,f] Yoshiaki Kawano,[a] Masaki Yamamoto,[a] Kunio Hirata[a*]

[a] Life Science Research Infrastructure Group, RIKEN SPring-8 Center, 1-1-1 Kouto, Sayo-cho, Sayo-gun, Hyogo 679-5198, Japan

[b] Structural Biology Division, Japan Synchrotron Radiation Research Institute, 1-1-1 Kouto, Sayo, Hyogo 679-5148, Japan

[c] Graduate School of Science and Technology, Nara Institute of Science and Technology, 8916-5 Takayama-cho, Ikoma, Nara 630-0192, Japan

[d] Japan Agency for Medical Research and Development-Core Research for Evolutional Science and Technology (AMED-CREST); Tokyo 100-0004, Japan

[e] Institute of Molecular Science, National Institute of Natural Sciences, 5-1 Higashiyama, Myodaiji, Okazaki, Aichi 444-8787, Japan

[f] Exploratory Research Center on Life and Living Systems, National Institute of Natural Sciences, 5-1 Higashiyama, Myodaiji, Okazaki, Aichi 444-8787, Japan

[‡] Current affiliation: Department of Chemistry, Faculty of Science and Technology, Keio University, 3-14-1 Hiyoshi, Kohoku, Yokohama, Kanagawa 223-8522, Japan

*Correspondence email: kunio.hirata@riken.jp

Synopsis Single-step intensity-based hierarchical clustering is demonstrated to allow the detection of structural polymorphs in the diffraction datasets obtained from multiple crystals. By splitting the datasets collected by continuous helical scan into several chunks, both inter and intra-crystal polymorphs can be successfully analyzed.

Abstract In macromolecular structure determination using X-ray diffraction from multiple crystals, the presence of different structures (structural polymorphs) necessitates the classification of diffraction data for appropriate structural analysis. Hierarchical clustering analysis (HCA) is a promising technique that has so far been used to extract isomorphous data, mainly for single structure determination. Although in principle the use of HCA can be extended to detect polymorphs, the absence of a reference for defining a 'similarity' threshold used for grouping the isomorphous datasets poses a challenge. Here, we have applied unit cell-based and intensity-based HCAs to the datasets of apo-trypsin and inhibitor-bound trypsin that were mixed post-data acquisition to investigate how effective HCA is in classifying polymorphous datasets. Single-step intensity-based HCA successfully classified polymorphs with a certain 'similarity' threshold. In datasets of several samples containing an unknown degree of structural heterogeneity, polymorphs could be identified by intensity-based

HCA using the suggested 'similarity' threshold. Polymorphs were also detected in single crystals using the data collected by the continuous helical scan method. These findings are expected to facilitate the determination of multiple structural snapshots by exploiting automated data collection and analysis.

Keywords: Polymorph analysis; High-data-rate macromolecular crystallography (HDRMX); Hierarchical clustering analysis (HCA); Automated structure analysis.

1. Introduction

Automation and acceleration of data collection at the macromolecular crystallography (MX) beamlines of synchrotron radiation facilities are yielding massive amounts of X-ray diffraction data. Such highly efficiency, high yield data acquisition is now becoming a major trend in MX, namely, high data-rate MX (HDRMX) (Bernstein *et al.*, 2020). HDRMX has been realized by the availability of highly brilliant X-ray beams (Ursby *et al.*, 2020; Sanchez-Weatherby *et al.*, 2019; Bowler *et al.*, 2015; Hirata *et al.*, 2013), fast readout of detectors (Casanas *et al.*, 2016), rapid sample exchange robots (Murakami *et al.*, 2020), and the application of automated measurement schemes (Zander *et al.*, 2015; Hirata *et al.*, 2019; Basu *et al.*, 2019; Bowler *et al.*, 2016). Furthermore, data reduction and structure analysis of the obtained datasets has also been automated in various pipelines (Yamashita *et al.*, 2018; Winter & McAuley, 2011; Wojdyr *et al.*, 2013). Finally, data management systems, including user interfaces for viewing these data, have been developed so that the experimenters can seamlessly manage and easily interpret the results of analyses from large amounts of data (Yamada *et al.*, 2013; Delagenière *et al.*, 2011; Fisher *et al.*, 2015).

Recently, structure determination using multiple crystals has been facilitated by various developments that include the automation and acceleration of data collection. In structure determination using microcrystals, especially from lipid cubic phase (LCP) crystals of membrane proteins, structures are sometimes determined using the small-wedge synchrotron crystallography (SWSX) approach. In the SWSX approach, the total oscillation range is reduced, but the number of photons per oscillation width is increased. Since each wedge dataset covers only a part of the reciprocal space, tens to hundreds of datasets must be measured from many microcrystals that are mounted in different orientations (Cherezov *et al.*, 2007; Rosenbaum *et al.*, 2007). Finally, the acquired datasets are merged and used to determine the structure. In the case of serial femtosecond crystallography (SFX) (Barends *et al.*, 2022) or serial synchrotron rotation crystallography (SSROX) (Gati *et al.*, 2014; Hasegawa *et al.*, 2017), a much larger number of datasets is required because every single frame covers only a small portion of reciprocal space, posing challenges in data collection and analysis. Here, the automation of data collection and analysis is crucial and has provided opportunities for expanding the target and achieving structure determination for diverse protein samples (Healey *et al.*, 2021).

During structural analysis using multiple crystals, it is crucial to select datasets that are sufficiently isomorphous. For example, if non-isomorphous datasets are merged in SAD phasing, it greatly

complicates searching for the heavy atom positions (Giordano *et al.*, 2012; Baba *et al.*, 2021). Hierarchical clustering analysis (HCA) is an approach that has been successfully utilized for extracting highly isomorphous datasets from multiple crystals. This approach has been implemented in the program *BLEND* (Foadi *et al.*, 2013) that conducts unit cell-based HCA, while HCA based on the correlation of diffraction intensities (also referred to as 'CC-based HCA') is realized in the program *ccCluster* (Santoni *et al.*, 2017). The automatic data processing pipeline *KAMO* implements both types of HCA.

Even when a structure can be solved using a single crystal, there are benefits to using multiple crystals for analyzing the structure. One benefit is in terms of attainable resolution. The resolution of a given structure can be improved as the number of datasets for merging increases, because the signal-to-noise ratio of weak diffraction spots is improved. Another benefit is linked to the analysis of polymorphs. Physiologically meaningful structural polymorphs have been found by classifying diffraction data from many crystals. Most earlier studies used HCA to extract highly isomorphic data for single structure determination. However, some studies have demonstrated that HCA can be a powerful tool to classify structural polymorphs (Nguyen *et al.*, 2022; Soares *et al.*, 2022). In principle, HCA does not require any prior information on how many data clusters (*i.e.*, number of 'polymorphs' in the context of MX) are involved in the entire dataset. In practice, however, there are generally two ways to interpret the results from the HCA. One approach determines a threshold for the degree of 'similarity' and clustered data below the threshold are considered to underly the same structure. The other approach decides the number of data clusters prior to analysis. Since it is impossible to know how many polymorphs are involved in the entire dataset, the former approach should be desirable. However, since there is no reference for deciding a 'similarity' threshold at present, it is necessary to analyze the merged datasets at each node exhaustively, and the results should be interpreted case-by-case. Therefore, we investigated the feasibility of assigning a 'similarity' threshold, which can be used to select the candidate data clusters where polymorphs may be identified.

Furthermore, we also investigated the usefulness of applying intensity-based HCA to helical scan data for capturing both inter and intra-crystal structural polymorphs. The helical scan, strictly referred to as a 'continuous helical scan,' was originally developed as a data collection scheme to avoid severe radiation damage (Flot *et al.*, 2010). In contrast to the conventional single-point oscillation scan, crystals collected by the helical scan method are translated during the data collection. Therefore, the dose for each crytal volume can be considered constant. Since each frame is acquired from a different point in the crystal, splitting the full dataset into several partial data sets (chunks) could be useful to observe structural differences present in the crystal by processing each chunk individually and classifying them by HCA. Indeed, using this approach, the structure determination was possible even from heterogeneous crystals (Katoh *et al.*, 2020).

In this paper, we sought to determine the 'similarity' threshold using *in silico* mixed datasets consisting of two different high-resolution datasets from test standard protein samples (trypsin). This threshold was then applied to two representative protein samples (nuclear transport receptor Transportin-1

and [NiFe]-hydrogenase maturation factor HypD) to evaluate whether the suggested 'similarity' threshold suitably classifies polymorphs. The results clearly indicated that the only intensity-based HCA can classify polymorphs. Based on the results of the test cases, the 'similarity' threshold was proposed to be sqrt(1-CC^2) ≤ 0.6. In the representative samples, polymorphs were successfully detected by intensity-based HCA with our suggested 'similarity' threshold.

2. Materials and Methods

2.1. Preparation of apo- and inhibitor-bound trypsin crystals

Bovine pancreas trypsin (Fujifilm Wako Pure Chemicals) was dissolved in 25 m*M* HEPES pH 7.0 with 5 m*M* $CaCl_2$ to a concentration of 30 mg ml^{-1}. The precipitant solution was 30% (*w/v*) PEG 3350, 0.1 *M* Tris-HCl pH 8.5, 0.2 *M* Li_2SO_4. Crystallization was performed at 293 K by the sitting-drop vapor diffusion method using MRC-II plates (SWISSCI), and 200 μm crystals appeared within a few days. Several crystals were harvested before adding the compound to obtain data for apo-form. The crystals were soaked in cryoprotectant, which contained 10% (*v/v*) ethylene glycol mixed with a crystallization buffer, then cryocooled in liquid nitrogen (Yamane *et al.*, 2011).

The inhibitor compound was directly added to the droplet on the crystallization plates using an Echo 650 acoustic liquid handler (Beckman Coulter). In this study, the following two inhibitors were used (Fig. S1); 4-Methoxybenzamidine and 5-Chlorotryptamine (hereinafter referred to as 'benzamidine' and 'tryptamine', respectively). Each inhibitor was added to the crystallization droplet at a final concentration of 1 m*M* containing 10% (*v/v*) dimethyl sulfoxide (DMSO). After addition of the inhibitor, the crystallization plate was placed at 293 K for an hour to allow sufficient inhibitor diffusion into the crystals. Inhibitor-bound trypsin crystals were fished from the crystallization plate, cryoprotected in a similar manner to apo-trypsin, and cryocooled in liquid nitrogen. DMSO concentration and the incubation time were determined based on the results of a preliminary study. In brief, several series of crystals with different DMSO concentrations and incubation times were prepared using apo-trypsin. Then, data were collected from these crystals to identify the conditions where the diffraction quality was not significantly degraded.

2.2. Diffraction data collection, data processing, and structure determination of trypsin

All diffraction data of trypsin crystals were collected at BL32XU, SPring-8, using an automated data collection system *ZOO* (Hirata *et al.*, 2019). Data were obtained from four crystals for apo-form, benzamidine-bound, and tryptamine-bound trypsin crystals, respectively. All datasets were acquired using a continuous helical scan scheme for 360° oscillation with the following experimental parameters; Beam size: 10 μm × 15 μm, Wavelength: 1 Å, Total dose/crystal: 10 MGy, Detector: EIGER X 9M (DECTRIS Co. Ltd.).

The obtained data were automatically processed by *XDS* (Kabsch, 2010) exploited in *KAMO* (Yamashita *et al.*, 2018). Subsequently, automated structural analysis was performed using *NABE*

(Matsuura *et al.*, unpublished), an automated structural analysis pipeline currently under development at SPring-8 MX-BLs. *NABE* provides an interface to manage all the merged data in clustering results generated by *KAMO* by summarizing the data statistics and the electron density map. *NABE* runs *DIMPLE* (Wojdyr *et al.*, 2013) on the data processed by *KAMO*, using the given template model for molecular replacement. If the amino acid residues and atom names are specified for a site of interest, *NABE* automatically generates pictures of protein model and resultant electron density maps ($2F_o$-F_c and F_o-F_c maps) around the selected site by using *Coot* (Emsley & Cowtan, 2004), *Raster3D* (Merritt & Bacon, 1997), and *ImageMagick* (The ImageMagick Development Team, 2021; Available at https://imagemagick.org). The pictures are not a static snapshot but a GIF image that swings, making it easier to see the surrounding environment, including the depth direction, which is difficult to perceive from a static image. After the above processes are completed, *NABE* returns a report HTML that tabulates the resolution of the obtained data, R_{Free}, *B*-factor, etc., from the results of *KAMO* and *DIMPLE*, along with the GIF image for each dataset. When multiple datasets are used, for example during SWSX measurements, *KAMO* classifies the diffraction data by HCA and then merges them in multiple nodes. Subsequently, *NABE* automatically performs the instantaneous data analysis for all these merged datasets.

Here, using the report from *NABE*, we listed the electron density map around the inhibitor binding site of trypsin and confirmed that the F_o-F_c density for inhibitors was not observed in the apo-trypsin. In contrast, F_o-F_c density for each inhibitor was observed for benzamidine-bound and tryptamine-bound trypsin (Fig. S1).

2.3. Clustering analysis using data from apo- and inhibitor-bound trypsin

In HCA, a 'similarity' between the datasets is represented as a 'distance' in the dendrogram. Similar datasets are linked within smaller distances, while other, more distantly related datasets are linked with longer distances. Supposing there are several structural polymorphs in the multiple datasets, each polymorph will make a cluster consisting of datasets within a certain 'distance' (referred to as 'similarity' threshold) in the dendrogram. In actual data, the number of polymorphs involved in the obtained dataset is unpredictable. Therefore, two apparently different datasets were investigated to determine a 'similarity' threshold for identifying polymorphs. For this purpose, we used high-resolution datasets from apo- and two different inhibitor-bound trypsin.

Two different parameter-based HCAs are implemented in *KAMO*: one is unit cell-based, and the other is intensity-based HCA. *KAMO* performs unit cell-based HCA using *BLEND*. Intensity-based HCA is performed based on the CC calculation by the *cctbx* (Grosse-Kunstleve *et al.*, 2002) method miller_array.correlation.coefficient and grouping by the *scipy* (Virtanen *et al.*, 2020) method cluster.hierarchy.dendrogram. The structural changes of protein molecules in the crystal possibly affect the unit cell constants or diffraction intensities. These two different parameter-based HCA are somewhat different in terms of similarity (isomorphism). In the unit cell-based HCA, the classification is based on the similarity of the crystal lattice, which reflects a more macroscopic aspect rather than the protein structures. In contrast, intensity-based HCA can detect much smaller structural changes.

Here, we examined how the two different datasets are classified by two different parameter-based HCAs: unit cell-based and intensity-based. To evaluate whether splitting the helical scan data enables polymorph analysis within the same crystals, collected data were divided into 30° chunks and individually processed using *KAMO* with the split_data_by_deg = 30.0 option. The test data set for clustering analysis was prepared by mixing the same number of diffraction data sets from two different structures. In this study, 360° helical scan data were used with division into 30° chunks. Here we used forty-eight 30° chunks of each structure, corresponding to datasets from four crystals. Two parameter-based HCAs were applied to the *in silico* mixed datasets consisting of 96 chunks from the following combinations of two datasets (48 + 48 chunks): (1) apo- and benzamidine-bound trypsin, and (2) benzamidine-bound and tryptamine-bound trypsin. Data were merged at each node, and the electron density map was depicted to evaluate the effect of data contamination. Molecular replacement was performed with the apo-trypsin template model (PDB ID: 3RXA). HCA and data merging were carried out using *KAMO*. Evaluation of the electron density map was performed using *NABE*.

In general, the definition of 'similarity' (or 'dissimilarity') between datasets and the linkage method to calculate the distance between clusters contribute significantly to the resultant dendrogram from HCA. For intensity-based HCA, a different definition of distance is used in *KAMO* and *ccCluster* as a default setting; sqrt(1-CC) is used in *KAMO* (Yamashita *et al.*, 2018), while sqrt(1-CC^2) is used in *ccCluster* (Santoni *et al.*, 2017). In this study, we used sqrt(1-CC^2) based on the preliminary investigations on the following distance definitions available in *KAMO*: 1-CC, sqrt(1-CC), and sqrt(1-CC^2). For the linkage method, we employed the Ward method, as it is empirically less prone to causing the 'chain effects' and 'inversions' of the dendrogram (Murtagh & Legendre, 2014). The program *BLEND* also adopts the Ward method for the same reason (Foadi *et al.*, 2013), while the program *ccCluster* uses the average linkage method instead. In intensity-based HCA implemented in *KAMO,* the Ward method is utilized as the default setting. Based on the preliminary investigations of the linkage method, we used the Ward method in this study.

2.4. Application to representative sample 1: Polymorph analysis of nuclear transport receptor Transportin-1 in complex with a nuclear localization signal peptide

To evaluate whether the 'similarity' threshold suggested from the investigations on trypsin datasets was sufficient, HCA with the proposed 'similarity' threshold was carried out in representative sample datasets.

Transportin-1 (Trn1) is one of the nuclear transport receptors which recognizes a nuclear localization signal (NLS) sequence harbored in cargo proteins and brings them into the nucleus. Detailed information about sample preparation of Trn1-NLS peptide complex is described in Supporting Information. Here we describe it briefly. The Trn-1 Δloop mutant was produced using an *Escherichia coli* expression system. Purification of Trn1 was performed using Glutathione Sepharose and anion exchange columns followed by size exclusion chromatography. NLS peptide of Trn1 (Eurofins) was dissolved in the purification buffer (110 m*M* potassium acetate, 200 m*M* HEPES-KOH, 10 m*M* DTT). Trn1-NLS peptide

complex (hereinafter referred to as 'Trn1-peptide complex') was prepared by mixing 5 mg ml^{-1} Trn1Δloop and 5 m*M* NLS peptide. Trn1-peptide complex crystals were obtained under the crystallization condition containing 0.5 *M* NaK phosphate pH 5.0. The obtained crystals were cryo-cooled in liquid nitrogen after cryoprotection with a 30% (*w/v*) glycerol-containing reservoir solution. Diffraction data were automatically collected at BL32XU, SPring-8 using *ZOO*. From each of the four crystals, 720° rotation data were acquired by the continuous helical scan scheme. Other experimental parameters were identical as performed for the trypsin crystals: Beam size: 10 μm × 15 μm, Wavelength: 1 Å, Total dose/crystal: 10 MGy, Detector: EIGER X 9M. The obtained 720° data was split into 30° chunks, and hierarchical clustering was applied. The electron density map was compared using *NABE* with the peptide-free structure model as a template model for MR. The peptide-free model was prepared prior to the clustering analysis by the following procedures: phasing by molecular replacement using the program *PHASER* (McCoy *et al.*, 2007) with a template model (PDB ID: 5YVI), followed by an iteration of refinement using *phenix.refine* (Liebschner *et al.*, 2019) and manual model building using *Coot*.

2.5. Application to representative sample 2: Polymorph analysis of [NiFe]-hydrogenase maturation factor HypD

HypD is one of the maturation factors of [NiFe]-hydrogenase and can form a complex with other maturation factors (Muraki *et al.*, 2019). The C360S variant of HypD from *Aquifex aeolicus* (hereinafter referred to as *Aa*HypD-C360S) was produced using an *Escherichia coli* expression system and purified using a cation exchange column with a sodium chloride gradient and size exclusion chromatography. *Aa*HypD-C360S crystals were obtained 16% (*w/v*) polyethylene glycol 3350, 0.1 *M* citrate buffer pH 5.6, and 1 m*M* dithiothreitol as a reservoir solution. The obtained crystals were cryo-cooled in liquid nitrogen after cryoprotection. Diffraction data were automatically collected at BL45XU, SPring-8 using *ZOO*. From each of the six crystals, 360° rotation data were acquired by a continuous helical scan scheme. Other experimental parameters are listed as follows; Beam size: 20 μm × 20 μm, Wavelength: 1 Å, Total dose/crystal: 10 MGy, Detector: PILATUS3 6M (DECTRIS Co. Ltd.). The obtained 360° data was split into 30° chunks, and hierarchical clustering was applied. Data were merged at largely separated data clusters that should exhibit structural polymorphisms. Evaluations of the electron density map were carried out by *NABE*. Before the analysis by *NABE*, a template model was prepared using *PHASER* (PDB ID for the initial model: 2Z1D), *REFMAC5* (Murshudov *et al.*, 2011), and *Coot*.

3. Results and Discussions

3.1. Test study: Classification of different trypsin datasets

To investigate whether HCA can classify polymorphic datasets, *in silico* mixed datasets were prepared, which consist of 48-chunks each from two different (apo- and benzamidine-bound) trypsin datasets resulting in a total of 96 chunks submitted to *KAMO*. The resolution of each chunk was approximately 1.2 Å. Each chunk contained about 50,000 reflections, and the overall completeness was about 40% and the space group was $P2_12_12_1$. *KAMO* rejected 13 chunks as outliers during pre-processing

leaving 83 chunks for HCA. Reflections up to 1.50 Å were used to calculate the correlation between the datasets in the intensity-based HCA.

3.1.1. Classification of diffraction data for apo-trypsin and benzamidine-bound trypsin

Unit cell-based and intensity-based HCAs were applied to the *in silico* mixed datasets, including apo- and inhibitor-bound trypsin (Figs. 1 and 2). In both HCA results, merged data at the top node (Cluster 82) exhibited no significant F_o-F_c density corresponding to benzamidine at 3.0σ, even though chunks of benzamidine-bound trypsin datasets were included in the mixed dataset (Figs. S3 and S4). This may be explained by the fact that the number of apo-trypsin datasets in the merged data was larger than that of benzamidine-bound trypsin as a consequence of outlier rejection by *KAMO* before HCA.

The largest linear cell variation (LCV) value (Foadi *et al.*, 2013), a characteristic quantity for unit cell variation, was 0.59%. Due to the slight differences in the unit cell constant between apo-trypsin and benzamidine-bound trypsin (Fig. S2), unit cell-based HCA did not succeed in fully separating apo-trypsin and benzamidine-bound trypsin datasets (Fig. 1). This implies that the unit cell-based HCA is less sensitive to a small lattice change, like the one found between apo-trypsin and benzamidine-bound trypsin crystal forms.

In a representative, practical case, well-classified clusters should be inferred from the electron density map since there is no label for polymorphs. Accordingly, we investigated the electron density map obtained from merged data at each node. The two different datasets appeared to be separated at the first branch (Clusters 78 and 81) based on the electron density map. Although both the apo- and benzamidine-bound chunks are mixed in these clusters, data contamination cannot be distinguished from the electron density map. Due to the rejection of outlier datasets during the merging process by *KAMO*, some of the contamination data chunks were eliminated. For example, although Cluster 78 has 2 apo-trypsin and 16 benzamidine-bound trypsin chunks immediately after the clustering, 10 chunks containing only benzamidine-bound trypsin datasets were merged as the final dataset resulting in a clear benzamidine electron density to be present (Table S1 and Fig. 2). In most of the other cases, even after the outlier rejection process, the final merged data still contained some contaminations (Table S1). For instance, the merged data at Cluster 77 consisted of 2 apo-trypsin and 11 benzamidine-bound trypsin chunks. However, a small number of contaminations did not affect the resulting electron density map (Fig. 1). Approximately 15% of the contamination did not affect the electron density map resulting from the dominant dataset in this test case.

In contrast to the above-described results, the intensity-based HCA (Fig. 2) succeeded to classify the two mixed datasets completely (Clusters 71 and 72). Apart from these two main nodes of apo- and benzamidine-bound trypsin crystal forms, some outliers were additionally excluded from the two main nodes into two minor nodes (Clusters. 74 and 80). Clear F_o-F_c density for benzamidine was observed at Cluster 72, while no significant F_o-F_c density of benzamidine was observed in other nodes at 3.0σ (Fig. S4). An exception to the near-perfect sorting of data chunks is the single benzamidine-bound chunk found

in Cluster 71, which is possibly a consequence of low benzamidine occupancy in this particular chunk. Apo- and benzamidine-bound trypsin datasets appeared to be clustered within a distance (sqrt(1-CC^2)) of 0.6. The successful sorting of apo- and benzamidine-bound data chunks demonstrates that intensity-based HCA can be effective to disentangle heterogeneous data chunks, even if differences in lattice dimensions are too minute to be classified by unit cell-based HCA.

3.1.2. Classification of two different inhibitor-bound trypsin datasets

Next, we tested HCA-based classification on datasets obtained from crystals of trypsin with two different inhibitors that have different skeletal formulas (Fig. S1) but share the same binding site; benzamidine and tryptamine.

Although clusters of homogenous datasets can be found for some nodes (*e.g.,* Clusters 74 and 76), overall, the two different inhibitor-bound data could not be successfully sorted by unit cell-based HCA (Fig. 3). The two inhibitor-bound trypsin have slightly different unit cell constants on the a-axis and c-axis (Fig. S2). The largest LCV value was 0.75%, slightly larger than the case for apo- and benzamidine-bound trypsin. This implies that a larger LCV value of 0.75% is still insufficient to classify the different trypsin datasets using the unit cell-based HCA.

Based on the electron density map (Fig. S5), the two different datasets appeared to be roughly separated at the first branch (Clusters 81 and 82). However, the electron density map at Cluster 80 clearly exhibited a mixture of both types of inhibitor-bound data. It appears to be difficult to distinguish the base skeletal structure from the electron density map. The merged data consisted of 6 benzamidine-bound chunks and 13 tryptamine-bound chunks, resulting in approximately 32% contamination against the dominant datasets (Table S2). At Cluster 77, the merged data consisted of 9 benzamidine-bound chunks and 4 tryptamine-bound chunks, where about 31% of contamination was against the prevailing dataset. Based on these results, about 30% contamination by a minor dataset might be a tolerable upper limit for obtaining an electron density map that allows initial model building.

Intensity-based HCA (Fig. 4) successfully sorted the data chunks into two homogenous datasets (Clusters 73 and 75), although two inhibitor-bound datasets were mixed at some small nodes in the right branch (Clusters 74, 79, and 81). The electron density maps obtained at Clusters 73 and 75 exhibited the clear F_o-F_c densities derived from benzamidine and tryptamine at 3.0σ, respectively (Fig. S6). In agreement with the results in the previous section, benzamidine-bound and tryptamine-bound chunks appeared clustered within the distance (sqrt(1-CC^2)) of 0.6, respectively.

3.1.3. Classification of apo-trypsin and two inhibitor-bound trypsin datasets

As shown in the earlier sections, two different datasets were classified using a single-step intensity-based HCA. However, more than three structural polymorphs may be found in practical cases. To test such a case, intensity-based HCA was applied to an *in silico* mixed datasets containing all three different trypsin datasets used in this study, namely apo-trypsin, benzamidine-bound, and tryptamine-

bound trypsin datasets.

The results showed that intensity-based HCA classified three different datasets almost perfectly (Fig. S8). The first branch of the dendrogram was divided into two branches, one containing only tryptamine-bound chunks (Cluster 115) and the other mainly containing apo- and benzamidine-bound chunks (Cluster 130). From the further clustering of the latter node, the node for apo-trypsin appeared at Cluster 114 and that for benzamidine-bound trypsin at Cluster 116. During the separation, some small nodes (Clusters 119, 120, and 128) appeared. These nodes are considered outliers because the number of chunks involved is less, and the distances between the chunks are relatively large compared to the other nodes. Although some inhibitor-bound chunks were mixed at the apo-trypsin dominant node (Cluster 114), it is possibly due to lower inhibitor occupancies. A similar result is also found in the intensity-based HCA on a mixed dataset including apo- and benzamidine-bound trypsin (Fig. 2). In agreement with the results described in the previous sections, different datasets appeared to be clustered within the distance (sqrt(1-CC^2)) of 0.6. Intriguingly, apo-trypsin and inhibitor-bound trypsin were not separated at the first bifurcation. This implies that the data separation in the dendrogram may not be an intuitive result.

3.1.4. 'Similarity threshold' suggested from the investigations on trypsin datasets

The investigations on trypsin datasets indicated that intensity-based HCA can successfully classify structural polymorphs. The results also suggested that a single-step intensity-based HCA could be sufficient when the variation in unit cell constant is small, for example, when the largest LCV value is less than 1%. In the dendrogram from intensity-based HCA on trypsin test cases (Figs. 2, 4, and S8), the same datasets appeared to be clustered within a distance (sqrt(1-CC^2)) of approximately 0.6, respectively. Based on the results, polymorphs could be identified by grouping the datasets using a single-step of intensity-based HCA with the suggested 'similarity' threshold (sqrt(1-CC^2) $\leq$ 0.6). Since multiple steps of clustering (Nguyen *et al.*, 2022) reduce the number of datasets in the final step by filtering the data during the clustering, fewer steps of clustering may be helpful when the number of total amount data is limited.

3.2. Applications to the representative samples

To evaluate whether the single-step of intensity-based HCA with our suggested 'similarity' threshold (sqrt(1-CC^2) $\leq$ 0.6) is useful for the detection of polymorphs in practical samples, we performed the intensity-based HCA and structure analysis on two representative examples: Trn1-peptide complex and *Aa*HypD-C360S. Here we selected the clusters that satisfy sqrt(1-CC^2) $\leq$ 0.6, alongside the completeness of the merged data being high enough to allow further structural analysis.

3.2.1. Diffraction data classification and polymorph analysis of the Trn1-peptide complex

Diffraction data of the Trn1-peptide complex were obtained using a helical scan for 720° rotation. Each dataset was divided into 30° chunks, yielding 96 chunks from 4 crystals. The resolution for each chunk was in the range of 3 to 4 Å. The number of reflections in each 30° chunk was approximately 60,000, and the overall completeness was about 25% and the space group was *C*2. Reflections up to 3.67 Å were

used to calculate the correlation between the datasets in the intensity-based HCA.

The obtained chunks were subjected to intensity-based HCA using *KAMO* (Fig. 5). Although some outliers were observed, the two major nodes (Clusters 72 and 76) were selected for further structural analysis. The electron density maps from these two nodes were significantly different (Fig. 6). There were two peptide-binding forms: one without any secondary structure (Form1) and the other with α-helix (Form2). These two peptide-binding forms were also observed when all chunks merged (Cluster 82). However, the F_o-F_c map for each peptide-binding form appeared to be less clear than the clustering results (Clusters 72 and 76). Although both peptide-binding forms appeared in each node, occupancies seemed different. The F_o-F_c map indicated that Form1 was dominant at Cluster 76 while Form2 was dominant at Cluster 72. This result demonstrated that intensity-based HCA with the suggested 'similarity' threshold ($\mathrm{sqrt}(1\text{-}CC^2) \leq 0.6$) could be useful for identifying polymorphs in a representative sample.

Since for the Trn1-peptide complex the variation of unit cell constants was more significant than that of trypsin (Fig. S9), we also applied unit cell-based HCA (Fig. S10). The largest LCV value for the Trn1-peptide complex was 4.03%, which was also significantly higher than that for trypsin (0.59%). The obtained electron density maps seemed different (Fig. S11), as observed in the results from intensity-based HCA (Fig. 6). However, the clustering result was a bit different. Form1-dominant nodes appeared in the left branch (Clusters 73 and 78), while both forms were observed in the right branch (Clusters 77 and 79). Form2-dominant node was not found in the result from unit cell-based HCA. Accordingly, a single-step intensity-based HCA seemed to classify the data better in the case even though the cell variation is significant.

Although the resolution was relatively low (lower than 3 Å), and the space group was not highly symmetric (*C2*) in the case of the Trn1-peptide complex, intensity-based HCA was adequate to identify two different peptide binding modes. The results imply that polymorph analysis can be performed on datasets exhibiting relatively low resolution and low symmetry space groups.

Another interesting finding is that the dominant peptide binding form was different even though the crystals were obtained in the same crystallization conditions. Furthermore, some crystals had both Form1-dominant and Form2-dominant chunks (*i.e.*, intra-crystal variation). This result implies that polymorphs not only in different crystals (inter-crystal) but also in the same crystals (intra-crystal) are discernible by collecting diffraction data via the continuous helical scan, significantly expanding the possibilities of polymorph analysis.

3.2.2. Diffraction data classification and polymorph analysis on *Aa*HypD-C360S

Using a helical scan, diffraction datasets of *Aa*HypD-C360S were acquired from six crystals applying 360° rotation per crystal. Each dataset was divided into 30° chunks, yielding 72 chunks from six crystals. The resolution for each chunk was approximately 1.6 Å. The number of reflections in each 30° chunk was about 100,000 reflections, overall completeness was about 45% and the space group was $P2_12_12_1$. For the intensity-based HCA, reflections up to 2.79 Å were used to calculate the correlation

between the datasets.

The dendrogram (Fig. 7) showed two major branches (Clusters 61 and 65), and both branches are further split into two or more nodes. Six nodes (Clusters 50, 51, 52, 54, 42, and 47) were selected for further analysis based on the suggested similarity threshold (sqrt(1-CC^2) $\leq$ 0.6) with sufficient completeness, except for Clusters 52 and 54, which are selected based on a less-stringent criterion (sqrt(1-CC^2) $\leq$ 0.8). Among the data from these nodes, some polymorphs that have differences around the N-terminal and the [4Fe-4S] regions were identified by examining the corresponding electron density maps (Figs. 8 and S12). Significant differences were found in Clusters 50 and 52. At Cluster 50, the N-terminal region was unfolded (referred to as 'unfolded' conformation) with no secondary structure and the occupancy of the [4Fe-4S] cluster decreased with the disorder of the surrounding area (Fig 8a and 8b). Whereas at Cluster 52, the N-terminal region was folded towards the protein side (referred to as 'folded' conformation), and the surrounding region around the [4Fe-4S] cluster was well-ordered (Fig. 8c and 8d). The electron density map in Cluster 51 (Fig. S12a and S12b) exhibited a similar trend in Cluster 50. However, the negative F_o-F_c peak of the [4Fe-4S] cluster was decreased in Cluster 51. The electron density map in Cluster 42 was similar to that in Cluster 52. However, the 'folded' N-terminal region was more evident in Cluster 52. Two different N-terminal conformations were highly related to the disorder around the [4Fe-4S] cluster. *B*-factor analysis clearly indicated that 'unfolded' conformation in N-terminal unstabilized [4Fe-4S] surrounding region (Fig. 9). From data at Cluster 54, a significantly high R_{Free} solution (R_{Free} > 0.4) was obtained. At Cluster 47, complete data was not obtained because most chunks were rejected by outlier rejection in *KAMO*. In this example, the most significant structural differences (N-terminal and [4Fe-4S] region) appeared to be separated at the first branch of the dendrogram (Clusters 61 and 65). During further separation, more slight differences (occupancies) seemed to be classified (Clusters 50 and 51, or Cluster 52 and 42).

Applying the suggested 'similarity' threshold, two major structural polymorphs were identified in *Aa*HypD-C360S. In addition, polymorphs were found from the crystals obtained under the same crystallization conditions. The results illustrate that proteins may have some metastable structures even under identical crystallization conditions.

3.3. Current limitations of intensity-based HCA and conceivable best practices for further applications

The results of the two representative samples demonstrated that intensity-based HCA with the proposed 'similarity' threshold (sqrt(1-CC^2) $\leq$ 0.6) can be a useful indicator to detect polymorphs in datasets obtained from multiple crystals. In addition, splitting the data collected by helical scan into several chunks could be beneficial for analyzing structural polymorphs within the same crystals. Even for well-known proteins whose structures have already been determined, structural polymorphs have possibly been overlooked. The simple criterion suggested in this study could be widely applied to the datasets acquired from multiple crystals, not only those collected by helical scan (*e.g.*, data obtained by the SWSX approach).

However, there is an explicit limitation for intensity-based HCA. A certain number of common reflections are required among the datasets for calculating CC. As a default setting in *KAMO*, at least three common reflections are required between each dataset. In SWSX, diffraction data is collected for 5°–20° rotation from each crystal, which results in fewer common reflections. The number of common reflections also decreases due to the lower resolution or crystallographic symmetry. In this study, the chunk size was set at 30°, where the number of common reflections is expected to be adequate.

To investigate the limitation on chunk size (rotation range), the number of common reflections and rejected data in different chunk sizes were plotted using the high-resolution trypsin dataset from 0.5° to 30° (Fig. S13). The number of chunks excluded from the CC calculation was drastically increased below 3°. When the chunk size was set to 0.5°, almost all data were rejected (99.0%). The result is consistent with the previous report on intensity-based HCA applied to SSX (serial synchrotron crystallography) data (2°/crystal) using *ccCluster* (Santoni *et al.*, 2017). Obviously, it is not realistic to apply the intensity-based HCA to single-frame data with extremely narrow or no oscillation data, such as collected by SFX (serial femtosecond crystallography) or SSROX (serial synchrotron rotation crystallography) approaches.

In addition, to investigate a sufficient number of common reflections for intensity-based HCA, the number of common reflections was plotted in different chunk sizes for the datasets used in this study (Fig. S14). Since the rejected data increased below 3° in the case of trypsin, log (Number of common reflections) ≧ 2.5 seems promising. If the resolution is relatively lower or crystallographic symmetry is not high, a large molecular weight could cover the number of reflections, as exhibited in the example of Trn1-peptide complex. If possible, partial helical scan or larger rotation data will help increase the common reflections for polymorph analysis with intensity-based HCA.

Unit cell-based HCA can still be useful when CC-based HCA is not available. Even for single-frame data, such as SFX data, unit cell constants are estimated. Therefore, unit cell-based HCA can be applied to any given diffraction dataset. In actual SFX data, datasets with different unit cell properties are sometimes mixed in the entire datasets (Nomura *et al.*, 2021). Considering a general case, unit cell-based HCA should first be applied to filter the dataset with different cell parameters. Although the unit cell-based HCA could not successfully classify polymorphs, they could be found because a small portion of contamination is often indistinguishable from the resulting electron density maps. Based on the results of trypsin, data contaminated with approximately 30% of a different structure was not distinguishable from that without any contamination according to the electron density map. In addition, as *KAMO* automatically excludes outliers during the data merging process, merged data may include less contamination. If the variation of unit cell constants is relatively small, say the largest LCV value is less than 1%, it is likely that unit cell-based HCA will not yield good classification results. However, even if CC-based HCA is unavailable, it is worth classifying by unit cell-based HCA because model building depends on the electron density map.

Although we classified polymorphs by a single-step intensity-based clustering, cell parameters should be considered for more accurate classification or general cases. From the result of unit cell-based

HCA for trypsin datasets, chunks from the same structure were separated into different branches (Figs. 1 and 3). If intensity-based HCA is further applied to the clusters obtained from unit cell-based HCA, the number of datasets remaining at the final stage of data merging may decrease. Thus, single-step clustering should be preferred when the total number of datasets is small. HCA with 2D parameters, including both cell parameters and intensity correlation, is under consideration for more effective single-step clustering.

4. Conclusions and outlook

We found that a single-step intensity-based HCA with the suggested 'similarity' threshold (sqrt(1-CC^2) ≤ 0.6) is useful for detecting polymorphs in multiple datasets based on the investigations of several samples. Furthermore, continuous helical data collection will be beneficial for considering polymorphs both in different crystals and within the same crystal. Although both helical scan and HCA had already been employed in MX experiments and analysis, we demonstrated some advantages in line with a current HDRMX trend. Since data are collected with a uniform dose in each frame by the helical scan, structural heterogeneity by dose accumulation could be less compared to the single-point oscillation. In addition, automated data collection may reduce the loss of isomorphism between the crystals caused by manual data collection. This could be due to possible variations within user defined experimental parameters (*i.e.*, exposure time). Hence, by utilizing the automated data collection, it would be possible to focus the discussion solely on the structural differences present in the crystals analyzed. Furthermore, highly efficient automated data collection will facilitate the analysis of many polymorphs with higher resolution since the number of measurable datasets per given beamtime has increased.

Our findings could be widely applied to other protein samples. Even though the resolution was relatively low (approximately 4 Å), physiologically meaningful polymorphs can be identified as exhibited in the example of Trn1-peptide complex. The representative examples also showed that protein molecules may exhibit different structures within the same crystal. In addition, polymorphs can be found from multiple crystals obtained under the same crystallization conditions in both actual cases. Determination of the 'similarity threshold' enables polymorph detection even if the existence of polymorphs is not expected from the sample preparation. It will also facilitate broader applications by automating the polymorph analysis with the proposed 'similarity' threshold.

The suggested polymorph analysis could help obtain various structural snapshots during the protein function process for elucidating the molecular mechanism. Determination of multiple structural snapshots will also contribute to more accurate structure prediction, as realized by *AlphaFold2* (Jumper *et al.*, 2021) or *RoseTTAFold* (Baek *et al.*, 2021). However, structural information on time series or reaction pathways among the identified polymorphs is not available by our approach. It may be complemented by molecular dynamics (MD) simulations. For instance, the free energy landscape analysis will help understand the dynamic structural mechanism during protein function (Oide *et al.*, 2020). Polymorph analysis will be further enhanced along with the techniques for inducting structural change, such as ligand mixing. Although time-resolved crystallography is a powerful tool for analyzing dynamics, the proposed polymorph analysis will help compensate for numerous difficulties in controlling such reactions.

Expanding the intensity-based HCA for single-frame data (from SFX or SSROX) should also be developed in the near future.

5. Availability

The here presented analysis can be performed anywhere by installing the program *KAMO*, which is available on GitHub (https://github.com/keitaroyam/yamtbx). The raw diffraction data used in this study are available from Zenode.

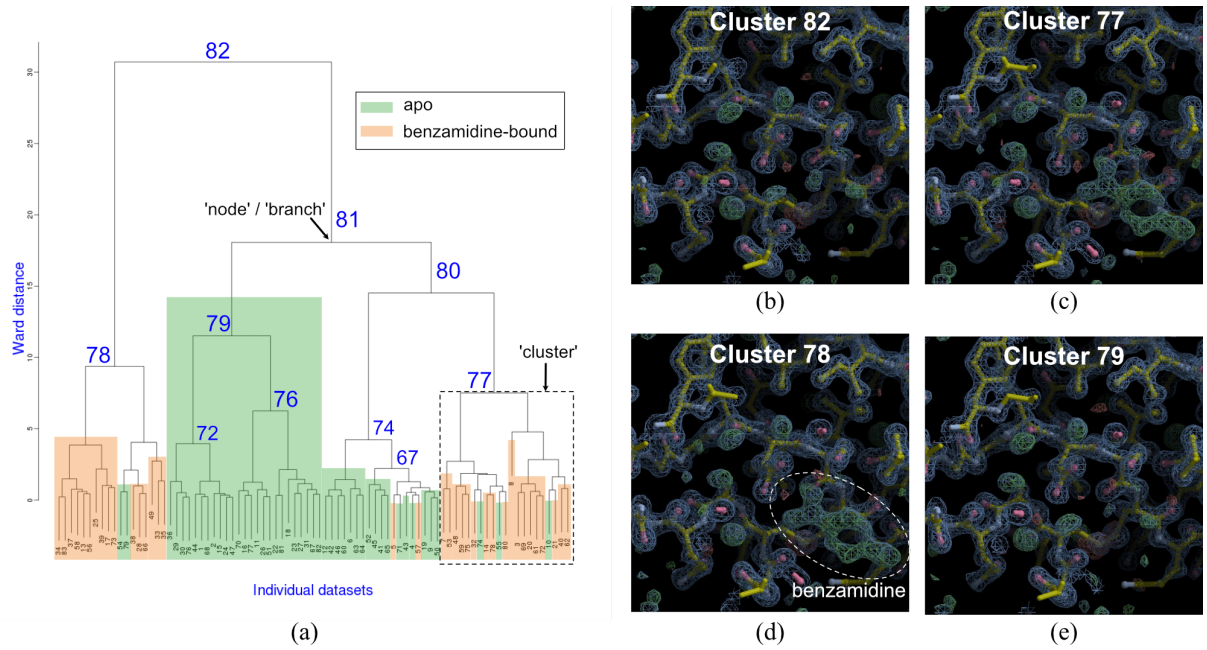

Figure 1 Result of unit cell-based HCA of *in silico* mixed datasets containing apo-trypsin and benzamidine-bound trypsin. (a) Resultant dendrogram. The definition of 'node', 'branch', and 'cluster' used in this study is illustrated in the dendrogram. Cluster numbers and data labels are depicted on the resultant dendrogram of unit cell-based HCA. The blue numbers indicate cluster numbers at each node. Chunks for apo-trypsin are shaded in green, and those for benzamidine-bound trypsin are colored in orange. (b)-(e) Electron density map around the inhibitor binding site of trypsin in different clusters. Contour level of $2F_o$-F_c map (blue mesh) is 1.0σ , and that of F_o-F_c map (green mesh) is 3.0σ. Maps were generated by *Coot* exploited in the *NABE* system. See also Fig. S3.

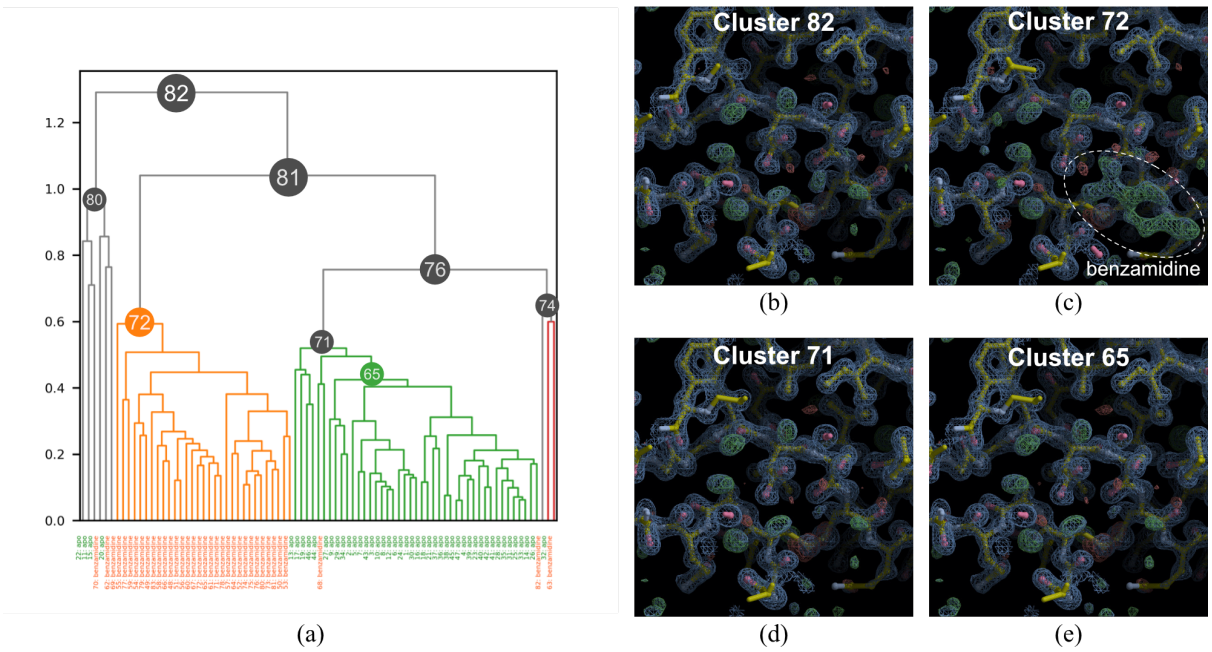

Figure 2 Result of intensity-based HCA on *in silico* mixed dataset containing apo-trypsin and benzamidine-bound trypsin. (a) Resultant dendrogram. Data labels are shown at the bottom: (green) apo-trypsin and (orange) benzamidine-bound trypsin. The color threshold for the dendrogram is set to 0.6. This color threshold classified apo- and benzamidine-bound trypsin data set well. The Dendrogram colored in gray indicates that the distance between these datasets is far, suggesting a different dataset. (b)-(e) Electron density map around the inhibitor-binding site obtained from the merged data in different clusters. Contour levels of $2F_o$-F_c map (blue mesh) and F_o-F_c map (green mesh) are 1.0σ and 3.0σ, respectively. Maps were generated by *Coot* exploited in the *NABE* system. See also Fig. S4.

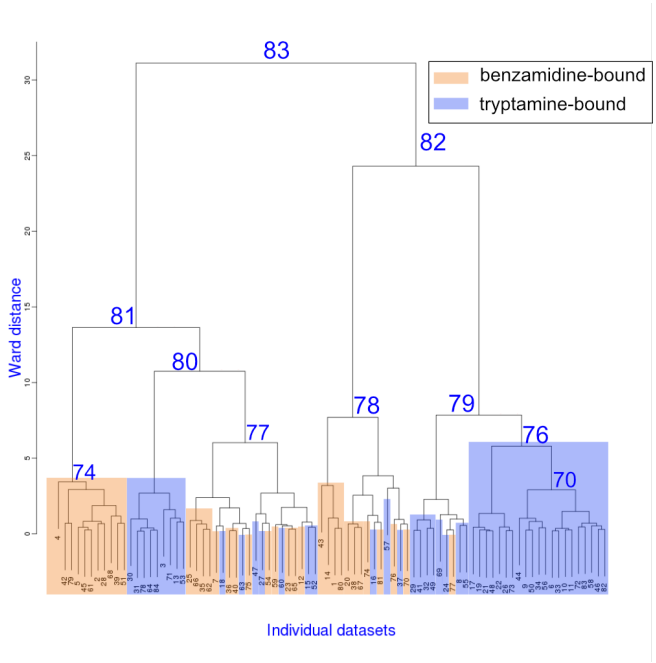

Figure 3 Dendrogram from unit cell-based clustering of mixed datasets including benzamidine-bound and tryptamine-bound trypsin. Cluster numbers and data labels are depicted on the resultant dendrogram of unit cell-based HCA. To evaluate the clustering effect, each cluster leaf is shaded according to the original dataset: (orange) benzamidine-bound and (blue) tryptamine-bound trypsin. The number labeled at each cluster node indicates the cluster number output from BLEND.

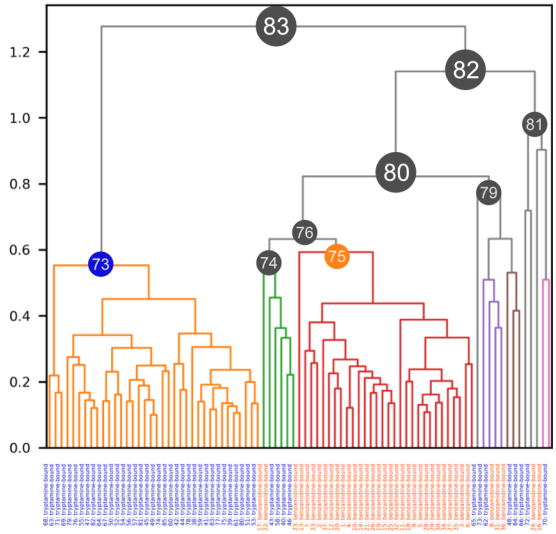

Figure 4 Dendrogram from intensity-based HCA of mixed datasets including benzamidine-bound and tryptamine-bound trypsin. Data labels at the bottom are (orange) benzamidine-bound and (blue) tryptamine-bound trypsin. The color threshold for the dendrogram is set to 0.6. With this color threshold, apo- and benzamidine-bound trypsin datasets were classified. The Dendrogram colored in gray indicates that the distance between these datasets is far, suggesting a different dataset.

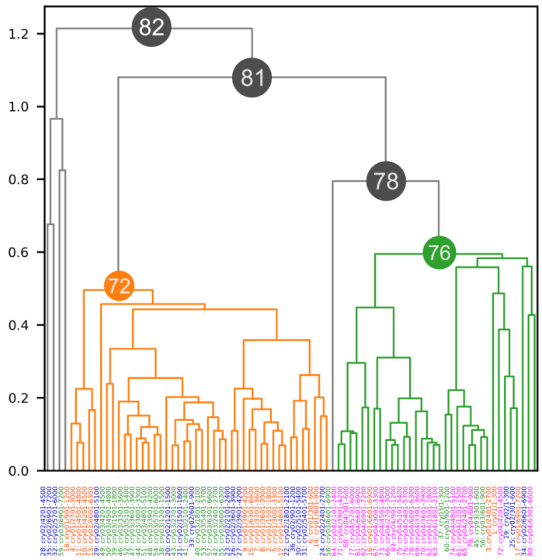

Figure 5 Dendrogram from intensity-based HCA for the Trn1-peptide complex. Data labels are shown at the bottom and colored by crystals. The color threshold for the dendrogram is set to 0.6.

Clusters 72 and 76 were used for further structural analysis because these two clusters appeared to have different structures (polymorphs).

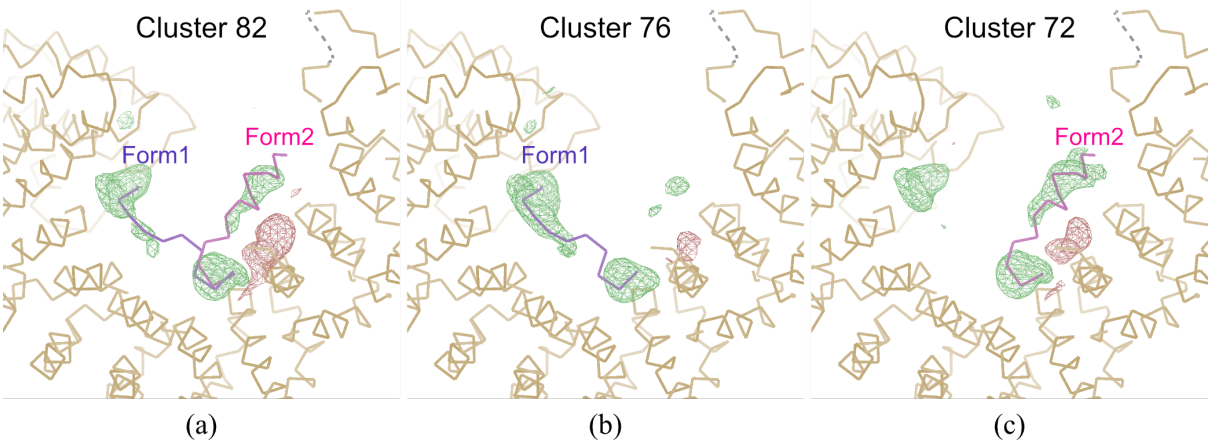

Figure 6 Peptide-omitted F_o-F_c map from different nodes resulted from intensity-based HCA for the Trn1-peptide complex. F_o-F_c maps calculated from merged data at (a) Cluster 82, (b) Cluster 76, and (c) Cluster 72 are depicted. The contour level for each figure is set to 3.0σ. Binding peptide was omitted during the map calculation. Figures were generated by *Coot*.

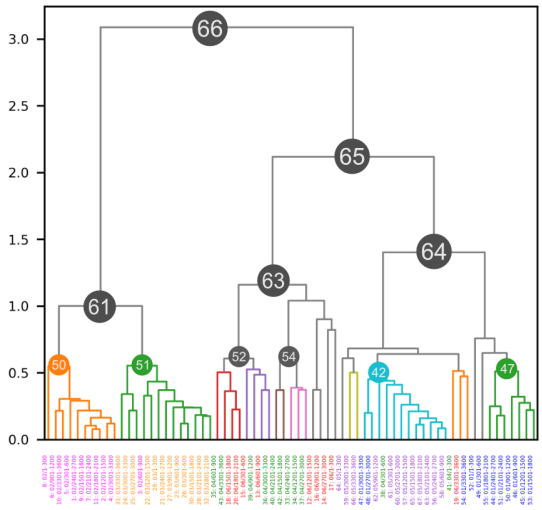

Figure 7 Dendrogram from intensity-based HCA on the *Aa*HypD-C360S variant. Data labels are shown at the bottom, colored by crystals. The color threshold for the dendrogram is set to 0.6. Due to the significant deviation among datasets, some clusters were not satisfied with enough completeness for further analysis. Accordingly, Clusters 52 and 54 were selected based on the results with the

threshold of 0.8. Each data cluster consists of chunks from one or two crystals, indicating that inter-crystal differences are more prominent than intra-crystal differences in the *Aa*HypD-C360S.

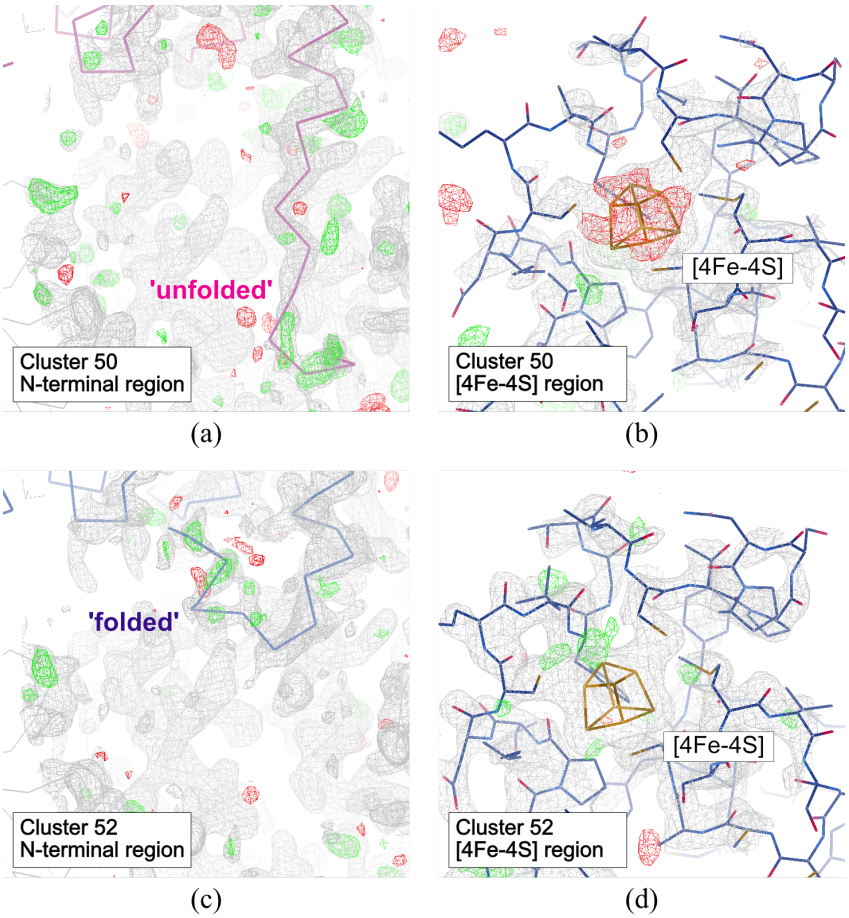

Figure 8 Electron density map around N-terminal region and [4Fe-4S] cluster obtained from merged data at different clusters: (a)-(b) Cluster 50 and (c)-(d) Cluster 52. The contour level for the $2F_o$-F_c map (gray mesh) is set to 1.0σ except for the [4Fe-4S] region in Cluster 52, where that is set to 1.5σ. The contour level for the F_o-F_c map is set to 3.0σ (green mesh: positive, red mesh: negative) in all figures. Figures were generated by Coot. Only the main chain is depicted in the N-terminal region: 'unfolded' (magenta), and 'folded' (purple). The variable N-terminal region (Ser7-Tyr12) was omitted and the occupancy for [4Fe-4S] cluster was set to 1.0 in map calculation. Figures were generated by *Coot*.

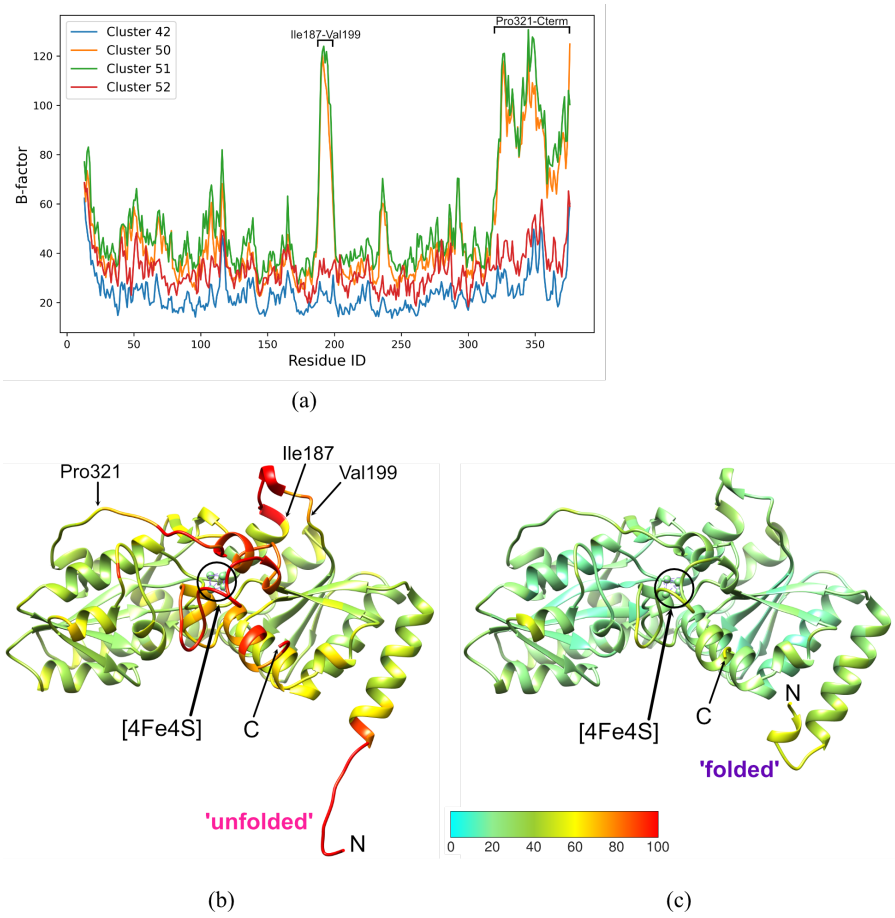

Figure 9 *B*-factor analysis on *Aa*HypD-C360S structures obtained from different clusters in intensity-based HCA. (a) Plot for *B*-factor of Cα atom in data from different clusters. (b)-(c) main-chain trace of *Aa*HypD-C360S with 'unfolded' N-terminal obtained from Cluster 50 (b) and with 'folded' N-terminal obtained from Cluster 52 (c). *B*-factor based coloring was applied using *Coot*. N-terminal and C-terminal are depicted in the figure as 'N' and 'C', respectively. The structure with 'unfolded' N-terminal showed significantly high *B*-factor around the [4Fe-4S] cluster. Figures were generated by *Chimera* (Pettersen *et al.*, 2004).

Acknowledgements We thank Keitaro Yamashita (MRC, LBL) for the helpful discussions. We also thank the BL45XU beamline staffs for assisting with X-ray crystallographic data collection. We sincerely thank Chai Gopalashingam and Christoph Gerle for critical reading of the manuscript and helpful suggestions. This research was supported by a Grant-in-Aid from the Japanese Ministry of Education, Cluture, Sports, Science, and Technology (21K06031) (STF), a Grant-in-Aid for Scientific Research on Innovative Areas Grant numbers JP19H05762 (SA), 19H05783(MY), the Japan Society for the Promotions of Science KAKENHI Grant Numbers, JP20K06517 (NM)), AMED-CREST under Grant Number 22gm1410010s0202 (STF), and the Platform Project for Supporting Drug Discovery and Life Science Research (Basis for Supporting Innovative Drug

Discovery and Life Science Research (BINDS)) from AMED under Grant Number JP21am0101072 (support number 1587) (STF) and JP20am0101070 (MY).

References

Baba, S., Matsuura, H., Kawamura, T., Sakai, N., Nakamura, Y., Kawano, Y., Mizuno, N., Kumasaka, T., Yamamoto, M. & Hirata, K. (2021). *J. Synchrotron Radiat.* **28**, 1284–1295.

Baek, M., DiMaio, F., Anishchenko, I., Dauparas, J., Ovchinnikov, S., Lee, G. R., Wang, J., Cong, Q., Kinch, L. N., Schaeffer, R. D., Millán, C., Park, H., Adams, C., Glassman, C. R., DeGiovanni, A., Pereira, J. H., Rodrigues, A. V., van Dijk, A. A., Ebrecht, A. C., Opperman, D. J., Sagmeister, T., Buhlheller, C., Pavkov-Keller, T., Rathinaswamy, M. K., Dalwadi, U., Yip, C. K., Burke, J. E., Garcia, K. C., Grishin, N. V., Adams, P. D., Read, R. J. & Baker, D. (2021). *Science*. **373**, 871–876.

Barends, T. R. M., Stauch, B., Cherezov, V. & Schlichting, I. (2022). *Nature Reviews Methods Primers*. **2**, 1–24.

Basu, S., Kaminski, J. W., Panepucci, E., Huang, C. Y., Warshamanage, R., Wang, M. & Wojdyla, J. A. (2019). *J. Synchrotron Radiat.* **26**, 244–252.

Bernstein, H. J., Andrews, L. C., Diaz, J. A., Jr, Jakoncic, J., Nguyen, T., Sauter, N. K., Soares, A. S., Wei, J. Y., Wlodek, M. R. & Xerri, M. A. (2020). *Struct Dyn*. **7**, 014302.

Bowler, M. W., Nurizzo, D., Barrett, R., Beteva, A., Bodin, M., Caserotto, H., Delagenière, S., Dobias, F., Flot, D., Giraud, T., Guichard, N., Guijarro, M., Lentini, M., Leonard, G. A., McSweeney, S., Oskarsson, M., Schmidt, W., Snigirev, A., von Stetten, D., Surr, J., Svensson, O., Theveneau, P. & Mueller-Dieckmann, C. (2015). *J. Synchrotron Radiat.* **22**, 1540–1547.

Bowler, M. W., Svensson, O. & Nurizzo, D. (2016). *Crystallography Rev.* **22**, 233–249.

Casanas, A., Warshamanage, R., Finke, A. D., Panepucci, E., Olieric, V., Nöll, A., Tampé, R., Brandstetter, S., Förster, A., Mueller, M., Schulze-Briese, C., Bunk, O. & Wang, M. (2016). *Acta Crystallogr D Struct Biol*. **72**, 1036–1048.

Cherezov, V., Rosenbaum, D. M., Hanson, M. A., Rasmussen, S. G. F., Thian, F. S., Kobilka, T. S., Choi, H.-J., Kuhn, P., Weis, W. I., Kobilka, B. K. & Stevens, R. C. (2007). *Science*. **318**, 1258–1265.

Delagenière, S., Brenchereau, P., Launer, L., Ashton, A. W., Leal, R., Veyrier, S., Gabadinho, J., Gordon, E. J., Jones, S. D., Levik, K. E., McSweeney, S. M., Monaco, S., Nanao, M., Spruce, D., Svensson, O., Walsh, M. A. & Leonard, G. A. (2011). *Bioinformatics*. **27**, 3186–3192.

Emsley, P. & Cowtan, K. (2004). *Acta Crystallogr. D Biol. Crystallogr.* **60**, 2126–2132.

Fisher, S. J., Levik, K. E., Williams, M. A., Ashton, A. W. & McAuley, K. E. (2015). *J. Appl. Crystallogr.* **48**, 927–932.

Foadi, J., Aller, P., Alguel, Y., Cameron, A., Axford, D., Owen, R. L., Armour, W., Waterman, D. G., Iwata, S. & Evans, G. (2013). *Acta Crystallogr. D Biol. Crystallogr.* **69**, 1617–1632.

Gati, C., Bourenkov, G., Klinge, M., Rehders, D., Stellato, F., Oberthür, D., Yefanov, O., Sommer, B. P., Mogk, S., Duszenko, M., Betzel, C., Schneider, T. R., Chapman, H. N. & Redecke, L. (2014). *IUCrJ*. **1**, 87–94.

Giordano, R., Leal, R. M. F., Bourenkov, G. P., McSweeney, S. & Popov, A. N. (2012). *Acta Crystallogr. D Biol. Crystallogr.* **68**, 649–658.

Grosse-Kunstleve, R. W., Sauter, N. K., Moriarty, N. W. & Adams, P. D. (2002). *J. Appl. Crystallogr.* **35**, 126–136.

Hasegawa, K., Yamashita, K., Murai, T., Nuemket, N., Hirata, K., Ueno, G., Ago, H., Nakatsu, T., Kumasaka, T. & Yamamoto, M. (2017). *J. Synchrotron Radiat.* **24**, 29–41.

Healey, R. D., Basu, S., Humm, A.-S., Leyrat, C., Cong, X., Golebiowski, J., Dupeux, F., Pica, A., Granier, S. & Márquez, J. A. (2021). *Cell Rep Methods*. **1**, None.

Hirata, K., Kawano, Y., Ueno, G., Hashimoto, K., Murakami, H., Hasegawa, K., Hikima, T., Kumasaka, T. & Yamamoto, M. (2013). *Journal of Physics: Conference Series*, Vol. *425*, p.

Hirata, K., Yamashita, K., Ueno, G., Kawano, Y., Hasegawa, K., Kumasaka, T. & Yamamoto, M. (2019). *Acta Crystallogr D Struct Biol*. **75**, 138–150.

Jumper, J., Evans, R., Pritzel, A., Green, T., Figurnov, M., Ronneberger, O., Tunyasuvunakool, K., Bates, R., Žídek, A., Potapenko, A., Bridgland, A., Meyer, C., Kohl, S. A. A., Ballard, A. J., Cowie, A., Romera-Paredes, B., Nikolov, S., Jain, R., Adler, J., Back, T., Petersen, S., Reiman, D., Clancy, E., Zielinski, M., Steinegger, M., Pacholska, M., Berghammer, T., Bodenstein, S., Silver, D., Vinyals, O., Senior, A. W., Kavukcuoglu, K., Kohli, P. & Hassabis, D. (2021). *Nature*.

Kabsch, W. (2010). *Acta Crystallogr. D Biol. Crystallogr.* **66**, 125–132.

Katoh, T., Sengoku, T., Hirata, K., Ogata, K. & Suga, H. (2020). *Nat. Chem.* **12**, 1081–1088.

Liebschner, D., Afonine, P. V., Baker, M. L., Bunkóczi, G., Chen, V. B., Croll, T. I., Hintze, B., Hung, L. W., Jain, S., McCoy, A. J., Moriarty, N. W., Oeffner, R. D., Poon, B. K., Prisant, M. G., Read, R. J., Richardson, J. S., Richardson, D. C., Sammito, M. D., Sobolev, O. V., Stockwell, D. H., Terwilliger, T. C., Urzhumtsev, A. G., Videau, L. L., Williams, C. J. & Adams, P. D. (2019). *Acta Crystallogr D Struct Biol*. **75**, 861–877.

McCoy, A. J., Grosse-Kunstleve, R. W., Adams, P. D., Winn, M. D., Storoni, L. C. & Read, R. J. (2007). *J. Appl. Crystallogr.* **40**, 658–674.

Merritt, E. A. & Bacon, D. J. (1997). *Methods in Enzymology*, Vol. *277*, pp. 505–524. Academic Press.

Murakami, H., Hasegawa, K., Ueno, G., Yagi, N., Yamamoto, M. & Kumasaka, T. (2020). *Acta Crystallogr D Struct Biol*. **76**, 155–165.

Muraki, N., Ishii, K., Uchiyama, S., Itoh, S. G., Okumura, H. & Aono, S. (2019). *Commun Biol*. **2**, 385.

Murshudov, G. N., Skubák, P., Lebedev, A. A., Pannu, N. S., Steiner, R. A., Nicholls, R. A., Winn, M. D., Long, F. & Vagin, A. A. (2011). *Acta Crystallogr. D Biol. Crystallogr.* **67**, 355–367.

Murtagh, F. & Legendre, P. (2014). *J. Classification*. **31**, 274–295.

Nguyen, T., Phan, K. L., Kozakov, D., Gabelli, S. B., Kreitler, D. F., Andrews, L. C., Jakoncic, J., Sweet, R. M., Soares, A. S. & Bernstein, H. J. (2022). *Acta Crystallogr D Struct Biol*. **78**, 268–277.

Nomura, T., Kimura, T., Kanematsu, Y., Yamada, D., Yamashita, K., Hirata, K., Ueno, G., Murakami, H., Hisano, T., Yamagiwa, R., Takeda, H., Gopalasingam, C., Kousaka, R., Yanagisawa, S., Shoji, O., Kumasaka, T., Yamamoto, M., Takano, Y., Sugimoto, H., Tosha, T., Kubo, M. & Shiro, Y. (2021). *Proc. Natl. Acad. Sci. U. S. A.* **118**,.

Oide, M., Kato, T., Oroguchi, T. & Nakasako, M. (2020). *FEBS J.* **287**, 3472–3493.

Pettersen, E. F., Goddard, T. D., Huang, C. C., Couch, G. S., Greenblatt, D. M., Meng, E. C. & Ferrin, T. E. (2004). *J. Comput. Chem.* **25**, 1605–1612.

Rosenbaum, D. M., Cherezov, V., Hanson, M. A., Rasmussen, S. G. F., Thian, F. S., Kobilka, T. S., Choi, H.-J., Yao, X.-J., Weis, W. I., Stevens, R. C. & Kobilka, B. K. (2007). *Science*. **318**, 1266–1273.

Sanchez-Weatherby, J., Sandy, J., Mikolajek, H., Lobley, C. M. C., Mazzorana, M., Kelly, J., Preece, G., Littlewood, R. & Sørensen, T. L. M. (2019). *J. Synchrotron Radiat.* **26**, 291–301.

Santoni, G., Zander, U., Mueller-Dieckmann, C., Leonard, G. & Popov, A. (2017). *J. Appl. Crystallogr.* **50**, 1844–1851.

Soares, A. S., Yamada, Y., Jakoncic, J., McSweeney, S., Sweet, R. M., Skinner, J., Foadi, J., Fuchs, M. R., Schneider, D. K., Shi, W., Andi, B., Andrews, L. C. & Bernstein, H. J. (2022). *Acta Crystallogr. Sect. F Struct. Biol. Cryst. Commun.* **78**, 281–288.

Ursby, T., Åhnberg, K., Appio, R., Aurelius, O., Barczyk, A., Bartalesi, A., Bjelčić, M., Bolmsten, F., Cerenius, Y., Doak, R. B., Eguiraun, M., Eriksson, T., Friel, R. J., Gorgisyan, I., Gross, A., Haghighat, V., Hennies, F., Jagudin, E., Norsk Jensen, B., Jeppsson, T., Kloos, M., Lidon-Simon, J., de Lima, G. M. A., Lizatovic, R., Lundin, M., Milan-Otero, A., Milas, M., Nan, J., Nardella, A., Rosborg, A., Shilova, A., Shoeman, R. L., Siewert, F., Sondhauss, P., Talibov, V. O., Tarawneh, H., Thånell, J., Thunnissen, M., Unge, J., Ward, C., Gonzalez, A. & Mueller, U. (2020). *J. Synchrotron Radiat.* **27**, 1415–1429.

Virtanen, P., Gommers, R., Oliphant, T. E., Haberland, M., Reddy, T., Cournapeau, D., Burovski, E., Peterson, P., Weckesser, W., Bright, J., van der Walt, S. J., Brett, M., Wilson, J., Millman, K. J., Mayorov, N., Nelson, A. R. J., Jones, E., Kern, R., Larson, E., Carey, C. J., Polat, İ., Feng, Y., Moore, E. W., VanderPlas, J., Laxalde, D., Perktold, J., Cimrman, R., Henriksen, I., Quintero, E. A., Harris, C. R., Archibald, A. M., Ribeiro, A. H., Pedregosa, F., van Mulbregt, P. & SciPy 1.0 Contributors (2020). *Nat. Methods*. **17**, 261–272.

Winter, G. & McAuley, K. E. (2011). *Methods*. **55**, 81–93.

Wojdyr, M., Keegan, R., Winter, G. & Ashton, A. (2013). *Acta Crystallogr. A*. **69**, 299–299.

Yamada, Y., Matsugaki, N., Chavas, L. M. G., Hiraki, M., Igarashi, N. & Wakatsuki, S. (2013). *J. Phys. Conf. Ser.* **425**, 012017.

Yamane, J., Yao, M., Zhou, Y., Hiramatsu, Y., Fujiwara, K., Yamaguchi, T., Yamaguchi, H., Togame, H., Tsujishita, H., Takemoto, H. & Tanaka, I. (2011). *J. Appl. Crystallogr.* **44**, 798–804.

Yamashita, K., Hirata, K. & Yamamoto, M. (2018). *Acta Crystallogr D Struct Biol*. **74**, 441–449.

Zander, U., Bourenkov, G., Popov, A. N., de Sanctis, D., Svensson, O., McCarthy, A. A., Round, E., Gordeliy, V., Mueller-Dieckmann, C. & Leonard, G. A. (2015). *Acta Crystallogr. D Biol. Crystallogr.* **71**, 2328–2343.